PIV measurement of separated flow over a blunt plate with different chord-to-thickness ratios

Liu Liu Shi, Ying Zheng Liu*, Jun Yu

Key Lab of Education Ministry for Power Machinery and Engineering, School of Mechanical Engineering, Shanghai Jiao Tong University, 800 Dongchuan road, Shanghai 200240, China

Abstract

The influence of the chord-to-thickness ratio (c/t) on the spatial characteristics of the separated shear layer over a blunt plate and the leading-edge vortices embedded in the separated shear layer was studied extensively using planar particle image velocimetry (PIV). Three systems corresponding to different shedding modes were chosen for the comparative study: $c/t = 3$, 6 and 9. The Reynolds number based on the plate's thickness (t) was $\mathrm{Re}_t = 1 \times 10^3$. A gigapixel CCD camera was used to acquire images with a spatial resolution of $0.06t \times 0.06t$ in the measurement range of $9.5t \times 4.5t$. Distributions of statistical quantities, such as the streamline pattern, streamwise velocity fluctuation intensity, shear stress and reverse flow intermittency, showed that the separated shear layer in the system with $c/t = 3$ did not reattach to the plate's surface, while the near-wake behind the trailing edge was highly unstable because the energetic leading-edge vortices were shed into the wake. The separated shear layer of the system with $c/t = 6$ periodically reattached to the plate's surface, which resulted in intensified fluctuations of the near wake behind the trailing edge. In the longest system ($c/t = 9$), the separated shear layer always reattached to the plate's surface far upstream from the trailing edge, which did not induce large fluctuations of the near wake. Furthermore, the proper orthogonal decomposition (POD) was extensively employed to filter the original velocity fields spatially to identify the large-scale vortices immersed in the separated shear layer easily. The distribution of the v-v correlation coefficients of the spatially filtered flow fields reflected the organized large-scale vortices in the three systems. The number of alternations of the positive and negative correlation coefficients across the flow field were determined to be 1, 2 and 3 for the systems with $c/t = 3$, 6 and 9, respectively; this is in agreement with the shedding mode of each system. The distribution of the swirling strength of the separated shear layer accurately determined the positions and structures of the large-scale vortices formed above the plate surface.

© 2010 Elsevier Ltd. All rights reserved.

Keywords: Separated flow; POD; Vortex shedding; Blunt plate

1. Introduction

Flow past an elongated blunt body, which has found its place in various practical applications that include high-rise buildings and bridge decks (Mills et al., 2003), has received widespread attention in the fluid mechanics community.

*Corresponding author. Tel./fax: +86 21 34206719.

E-mail address: yzliu@sjtu.edu.cn (Y.Z. Liu).

Nomenclature		$\langle u'v' \rangle$	shear stress ($m^2 s^{-2}$)
		x	streamwise coordinate (m)
c	chord of the blunt plate (m)	x_0	streamwise coordinate of the reference point
d	diameter (μm)		(m)
D	velocity gradient tensor	y	lateral coordinate (m)
f	frequency (Hz)	y_0	lateral coordinate of the reference point (m)
M	number of snapshots	γ_t	reverse-flow intermittency factor
m	vortex shedding mode	δ_ω	vorticity thickness (m)
R_{vv}	two-point spatial v–v correlation	λ	Eigenvalue
Re_t	Reynolds number based on thickness of the	λ_{ci}	swirling strength (m)
	blunt plate	λ_x	streamwise wavelength
S_c	Strouhal number based on the chord of the	ρ	density ($kg\,m^{-3}$)
	blunt plate		
t	thickness of the blunt plate (m)	*Abbreviations*	
u	time-averaged streamwise velocity ($m\,s^{-1}$)		
u_{rms}	root mean square of the streamwise velocity	PIV	particle image velocimetry
	($m\,s^{-1}$)	POD	proper orthogonal decomposition
U_0	free-stream velocity ($m\,s^{-1}$)		

Vortex shedding from a short blunt body placed in a uniform stream is considered a Karman vortex street, which results from strong interaction between two separated shear layers. However, elongating the plate in the streamwise direction weakens the interaction and introduces considerable complexity into the features of the separated shear layers, which are highly related to those of the impinging shear layer and the vortices that are shed from the leading edge. The characteristics of the shedding vortices superimposed in the separated shear layer above the plate play a significant role in flow-induced structural vibration and acoustics (Ohya et al., 1992). Understanding the characteristics of vortex shedding from an elongated blunt body and the influence of vortex shedding on the separated shear layer is highly desirable.

Vortex shedding from the elongated blunt body with square leading and trailing edges has been studied by many researchers (Parker and Welsh, 1983; Stokes and Welsh, 1986; Nakamura et al., 1991). Nakamura and Nakashima (1986) proposed the impinging shear-layer instability mechanism to explain vortex shedding from the elongated blunt body, which results from a single separated shear layer in an unstable state in the presence of a sharp trailing edge. The well-documented experiments performed with a Reynolds number of 10^3 by Nakamura et al. (1991) comprehensively described the dependency (Fig. 1) of vortex shedding from an elongated blunt plate on the chord-to-thickness ratio c/t, where c and t are the chord and thickness of the plate, respectively. The velocity measurements using multi-channel I
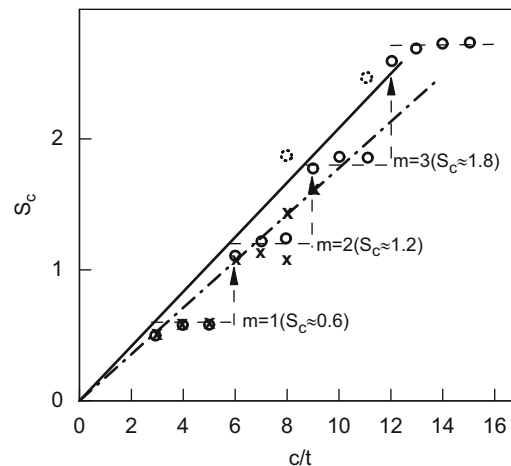

Fig. 1. Dependency of vortex shedding from an elongated blunt plate on the chord-to-thickness ratio c/t (Nakamura et al., 1991; Ohya et al., 1992).

hotwires determined that the Strouhal number $S_c = f \cdot c/U_0$ is approximately constant at 0.6 for $3c/t5$, while a further increase of c/t up to 15 results in a stepwise increase of S_c to $0.6m$; here, the integral multiplier m corresponds to the number of vortices that form in the separated shear layer to cover the plate's chord (Nakamura et al., 1991). This stepwise variation of S_c disappears for natural shedding at Reynolds numbers that exceed 2.0×10^3 (Mills et al., 2003). Ohya et al. (1992) claimed that the separated flows over the flat plates with different configurations, $3c/t5$, $6c/t8$ and $9c/t11$, are grouped into the first ($m = 1$), second ($m = 2$) and third ($m = 3$) branches of vortex shedding, respectively. The numerical results (Ohya et al., 1992) showed that the shortest plate in each branch, e.g., $c/t = 3$, 6 and 9, corresponds to regular vortex shedding, while increasing c/t gives rise to irregularities in vortex shedding. Subsequently, based on hot-wire measurements of the flow at low Reynolds numbers, $200\text{-}10^3$, Nakamura et al. (1996) found that the transition from Karman shedding to impinging shear-layer instability occurs at Reynolds numbers over 300. However, a more accurate explanation of vortex shedding from an elongated blunt body and the stepwise variation of S_c with increasing c/t was determined to be the impinging leading-edge vortex instability mechanism (Naudascher and Rockwell, 1994), which clarifies the interaction between vortices shed from the leading-edge separation bubble and the sharp trailing edge for a configuration with $c/t > 7$. Subsequently, the dominant role of the impinging leading-edge vortex instability mechanism in vortex shedding from elongated rectangular, H and T sections was confirmed by Nakamura et al. (1996). Recently, particle image velocimetry (PIV) measurements of the forced flow around long rectangular cylinders ($c/t = 6\text{–}10$) with Re = 490 revealed that the leading- and trailing-edge shedding vortices of like sign at the trailing edge merge before being shed into the wake (Mills et al., 2003). Using a hot-wire probe, Yaghoubi and Mahmoodi (2004) measured the time-averaged quantities (velocity, turbulence intensity and reattachment point) of the separated and reattaching flow for different configurations of long blunt plates ($c/t = 4\text{–}9$). These results illustrated the dominant presence of the leading-edge shedding vortices above the blunt plate. However, few experimental studies (Mills et al., 2003) have been performed to determine the influence of the chord-to-thickness ratio of the blunt plate on the global characteristics of the separated shear layer and the leading-edge shedding vortices embedded in the separated shear layers.

The main objective of the present study is to elucidate the global characteristics of the separated shear layer with a stepwise variation of S_c and determine the spatial characteristics of the leading-edge shedding vortices. Towards this end, three systems were selected to compare the separated shear layers with a Reynolds number $Re_t = 1 \times 10^3$: $c/t = 3$, 6 and 9, which correspond to the first, second and third branches of vortex shedding, respectively (Ohya et al., 1992). The separated shear layer above the blunt plate was measured using planar particle image velocimetry (PIV). A high-image-density CCD camera (RedLake, USA) with gigapixels was employed in the experiments to provide a detailed view of the separated shear layer at the spatial resolution of $0.06t \times 0.06t$. Detailed information on the spatial characteristics of the separated flow over the blunt plate is provided in terms of distributions of the statistical quantities, e.g., streamwise velocity fluctuation intensity, shear stress and reverse flow intermittency. The features of the leading-edge shedding vortices were obtained by spatially correlating the vertical velocity fluctuations and swirling strength distribution of the separated shear layer.

2. Experimental apparatus

Experiments were performed in the recirculating open water channel shown in Fig. 2(a); the flow was circulated by a magnetic drive centrifugal pump (Iwaki, Japan) to avoid facility structure vibration. A settling chamber, a honeycomb, 6 screens and a contraction section were placed in sequence to ensure flow homogeneity. The dimensions of the test section were 150 mm (width) × 200 mm (height) × 1050 mm (length). A blunt plate ($t = 8$ mm) spanning the entire width of the test-section was placed in the water channel at the middle depth; the free-stream velocity was maintained at 0.125 m/s, which results in a Reynolds number $Re_t = 1 \times 10^3$ based on the plate thickness. The free-stream turbulence intensity was less than 2%. Three systems with different chord-to-thickness ratios, $c/t = 3$, 6 and 9, were chosen for comparison. The sidewalls of the water channel and the blunt plate were made of plexiglas for easy optical access in PIV measurements.

The separated shear layer over the blunt plate was measured using planar PIV. Glass beads ($\rho \approx 1.05$ kg/m^3, $d \approx 10$ μm) were used as tracer particles; the middle plane was illuminated by a 1.8-W continuous-wave semiconductor laser. A gigapixel (4000 × 2600 pixels) CCD camera (IPX 11M, USA) was used to acquire the images; image distortion was suppressed by using an 85-mm lens (PC Micro Nikon, Japan). The laser was modulated to give 5-ms pulses and synchronized to the CCD camera with the use of a pulse delay generator. The inherent inter-channel time interval of the generator is on the order of picoseconds, which results in good synchronization between the CCD camera and the laser. The appropriate combination of cylindrical lenses was fitted to the compact laser to produce a 1-mm-thick light sheet along the center of the plate. As shown in Fig. 2(b), measurements were taken in the range of $9.5t \times 4.5t$ for the
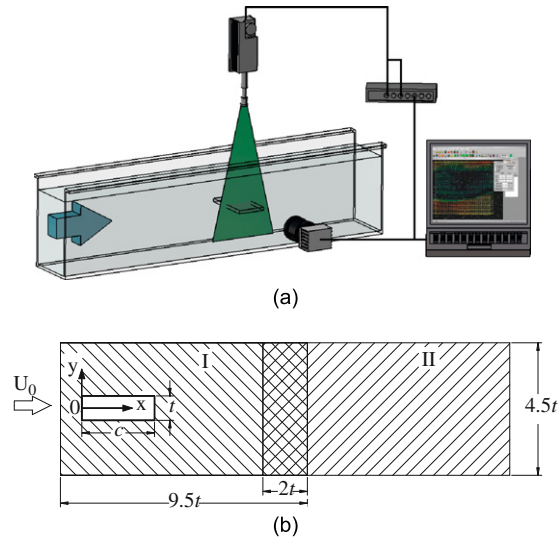
Fig. 2. Schematic of (a) the experimental set-up and (b) the measurement region.

system with $c/t = 3$ and two adjacent regions ($9.5t \times 4.5t$) for the other two systems ($c/t = 6$ and 9) by adjusting the light sheet and the camera; in the latter two systems, the two regions overlapped by $2t$ in the streamwise direction to obtain a combined distribution of the time-averaged quantities easily. In each measurement region, a total of 500 velocity fields were acquired. The interrogation window size was 64×64 pixels with 62.5% overlap, which yielded a measurement grid of velocity vectors with a spacing of 0.47 mm × 0.47 mm. The standard cross-correlation algorithm, in combination with window offset (Westerweel et al., 1997), sub-pixel recognition by Gaussian fitting (Yasuhiko et al., 2000) and sub-region distortion, was used to improve the signal-to-noise ratio.

3. Results and discussion

3.1. Time-mean flow field

A preliminary view of the influence of the chord-to-thickness ratio on the separated shear layer can be obtained by plotting time-mean streamline pattern in Fig. 3; contours of the time-mean streamwise velocity component are superimposed to assist flow structure interpretation. For the system with $c/t = 3$ (Fig. 3(a)), the flow separates immediately from the leading edge of the plate without reattaching to the plate's surface. This finding is in agreement with the results given by Parker and Welsh (1983). The near-wall region throughout the plate experiences high reverse flow, which peaks at $u/U_0 = -0.145$ near the trailing edge. At the station $x/t = 2.5$, a slender separation bubble is detected $0.3t$ away from the plate surface. Behind the trailing edge, two large counter-rotating recirculation zones form in the wake with approximate dimensions of $1t$ and $2.5t$ in the longitudinal and streamwise directions, respectively. The reverse flow between the recirculation zones peaks at $u/U_0 = -0.195$ and $x/t = 4$. The end of the time-mean recirculation zones, which is estimated by locating the saddle point in the streamwise pattern, is determined to be approximately $x/t = 5.35$. The prominent interconnection of the streamlines between the recirculation zone and the separation bubble above the plate reflects the strong interaction of the wake and the separated shear layer. When the plate is elongated to $c/t = 6$ (Fig. 3(b)), the time-mean separated shear layer reattaches to the plate's surface at $x/t = 4.9$, which causes a slender separation bubble to form near the wall. Previous studies regarding separated and reattaching flow over a blunt body (Kiya and Sasaki, 1985; Liu et al., 2005) show that the instantaneous reattachment point varies by $\pm 1t$ with the time-mean reattachment position as the reference. The fact that the time-mean reattachment point in the system with $c/t = 6$ is relatively close to the training edge illustrates the periodic impingement of the separated shear layer combined with large variation of the instantaneous reattaching point that significantly influences the wake region; a considerable disturbance associated with the downward movement of the fluid flow in the vortex structures is exerted. This phenomenon is described further in Figs. 4 and 5. Accordingly, no regular time-mean recirculation zone forms behind the plate. For the system with $c/t = 9$ (Fig. 3(c)), the separation bubble immediately behind the leading edge
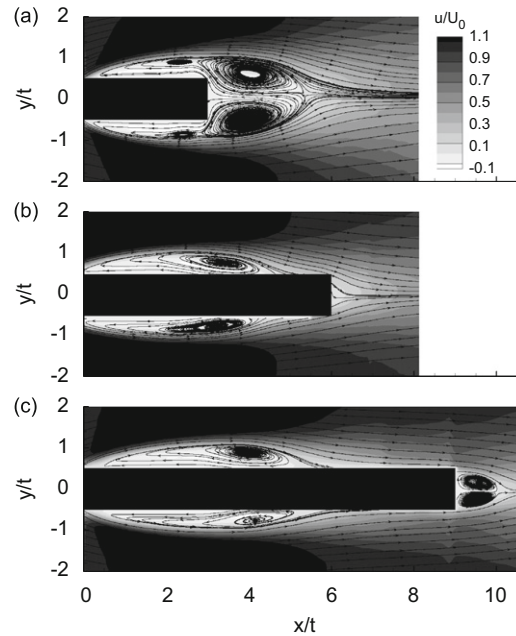
Fig. 3. Streamline pattern and streamwise velocity distribution of the time-averaged flow field: (a) $c/t = 3$, (b) $c/t = 6$ and (c) $c/t = 9$.

slightly extends downstream, and the time-mean reattachment point is determined to be approximately $x/t = 5.3$. In the system with $c/t = 9$, the separated shear layers are always reattached to the plate's surface (Parker and Welsh, 1983), which indicates that the wake region is almost immune to the reattached shear layer. Behind the trailing edge in the wake, two counter-rotating recirculation zones form with a reduced size ($1t$ long and $0.5t$ thick). The reverse flow inside the attached separation bubble peaks at $x/t = 3.8$ and reaches a value of $u/U_0 = -0.125$. Downstream from the separation bubble, the dominance of the leading-edge shedding vortices considerably influences the redeveloping boundary layer, which reduces the speed of the fluid near the plate's surface.

3.2. Statistical quantities

A more straightforward view of the reattachment state of the separated shear layer is obtained by plotting the contour of the reverse flow intermittency factor in Fig. 4. Here, the reverse flow intermittency factor γ_t is defined as the fraction of instances during which the flow at a given position is reversed. Thus, a value of $\gamma_t = 0$ at a given location means that the local fluid always flows downstream, while a value of $\gamma_t = 1.0$ corresponds to the fact that the local fluid always flows upstream. For the system with $c/t = 3$ (Fig. 4(a)), the fluid flow in the vicinity of the plate's surface is fully reversed in the region $x/t < 1.5$, which indicates that the separated shear layer in the first half of the plate is very stable. However, the fluid flow in the rear half of the plate is intermittently reversed, which might be a result of the growing leading-edge vortices. Far downstream from the plate, at the station $x/t = 8$, a slight reverse in the fluid flow in the main wake is still discerned. This phenomenon results from the shedding of leading-edge vortices into the wake and the formation of the Karman-like vortex street. The intermittency in the wake peaks at $\gamma_t = 0.85$ at the station $x/t = 4$. The streamwise position with $\gamma_t = 0.5$ is detected at the station $x/t = 5.35$, which is regarded as the boundary of the time-mean recirculation zones. For the system with $c/t = 6$ (Fig. 4(b)), the reverse flow intermittency factor of the fluid near the plate's surface is maintained at 1.0 for $x/t < 2$ and then gradually decreased to $\gamma_t \approx 0.15$ at the trailing edge corner, because of the periodic reattachment of the separated shear layer to the trailing edge and irregular trailing edge vortex shedding (Nakamura et al., 1991). The wake region with flow reversal is reduced to $1.5t$ in length. With a further increase to $c/t = 9$ (Fig. 4(c)), the distribution of the reverse flow intermittency factor is roughly similar to that of the system with $c/t = 6$, with the only prominent exception of $\gamma_t \equiv 0$ in the bulk region of the range $7 < x/t < 9$. This confirms that the separated shear layer always reattaches to the surface of the plate (Nakamura et al., 1991). In the near wake region behind the trailing edge of the plate, the reversal extent of the fluid is larger than that in the system with $c/t = 6$, which is attributed to the fact that the new boundary layer attached to the long plate has redeveloped and regular
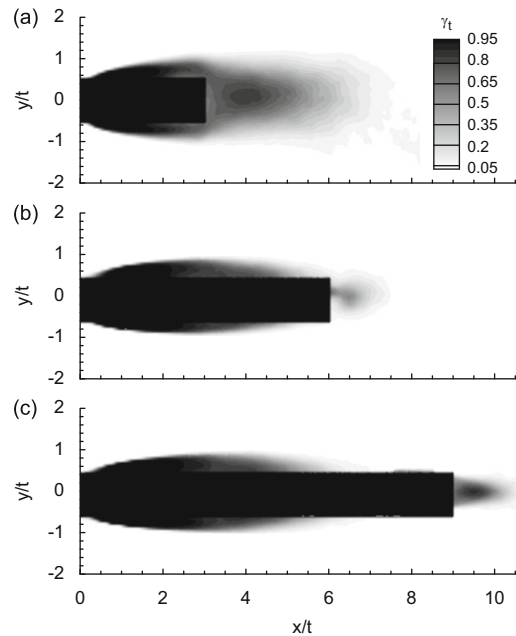
Fig. 4. Contour plot of reverse flow intermittency: (a) $c/t = 3$, (b) $c/t = 6$ and (c) $c/t = 9$.

trailing-edge vortex shedding occurs. Furthermore, a close comparison of the distribution of the reverse flow intermittency in the coverage of the plate indicates that the stable reversal region ($\gamma_t = 1.0$) is slightly extended in the streamwise direction with increasing c/t. From $c/t = 3$ to $c/t = 6$, the extension of the stable reversal region is partially a result of the suppression of the interaction of the two separated shear layers; whereas, the further extension of the region when c/t is increased to 9 might result from weakened interference from the sharp trailing edge (Hourigan et al., 2001).

To determine the near-wall behavior of the separated shear layer in the systems with $c/t = 6$ and 9 accurately, the streamwise variations of the near-wall time-averaged streamwise velocity and the reverse flow intermittency factor were extracted from Fig. 4 along $y/t = 0.6$ and plotted in Fig. 5. The time-averaged reattachment point ($\gamma_t = 0.5$) is determined to be $x/t = 4.9$ and 5.3 for the systems with $c/t = 6$ and 9, respectively. For the system with $c/t = 6$, the sharp variation of γ_t near the time-averaged reattachment point is observed, and near the trailing edge, γ_t is still greater than 0.15 because of the large variation of the instantaneous reattachment point and modulation of the vortical structures on the near-wall flow (Kiya and Sasaki, 1985). However, in the system with $c/t = 9$, large variation of γ_t was detected in the region $4 < x/t < 8$, and further downstream to the trailing edge, γ_t is constant with a value of zero. This result provides solid evidence for the claim by Parker and Welsh (1983) that the separated shear layer is periodically reattached to the trailing edge under the dominant modulation of the flapping separation bubble for the system with $c/t = 6$, while it is always reattached to the plate surface in the region $x/t < 8$ in the system with $c/t = 9$. It is important to note that in the system with $c/t = 6$, the reverse flow intermittency sharply decreases in the region $1.9 < x/t < 2.9$ and is nearly constant in the region $2.9 < x/t < 4$; the magnitude of the reversed flow reaches a maximum of $u/U_0 = -0.15$ at $x/t = 4$. Similar distributions of the reverse flow intermittency and the peaked reverse flow are observed in the system with $c/t = 9$ (Fig. 5(b)). These particular features can be explained by inspecting one realization of the instantaneous flow field shown in Fig. 6. As shown in Fig. 6((b), (c)), the leading-edge vortex grows rapidly in size, reaching the large-scale state near the stations $x/t = 2.4$ and 2.6 for the systems with $c/t = 6$ and 9, respectively. This attaching vortex considerably influences the near-wall fluid, which is closely related to the sharp reduction in the reverse flow intermittency for $1.9 < x/t < 2.9$ for both systems, as shown in Fig. 5((b), (c)). For the systems with $c/t = 6$ and 9, close inspection of the spatial extent of the downstream larger vortex located at the station $x/t = 4$ in Fig. 6((b), (c)) indicates that the attaching vortex is convected downstream parallel to the plate surface, which causes flattened variation of the reverse flow intermittency in the range $2.9 x/t 4$ (Fig. 5). In the system with $c/t = 6$, the separated shear layer instantaneously reattaches to the plate's surface near the station $x/t = 5$; the rapid reduction of the reverse flow intermittency in the range $x/t > 4$ (Fig. 5(a)) results from periodic reattachment of the separated shear layer near the trailing edge. However, for the system with $c/t = 9$, a prominent disruption of the vortex is observed in the reattachment zone in the instantaneous realization, as shown in Fig. 6(c); this process, in combination with the flapping motion of the
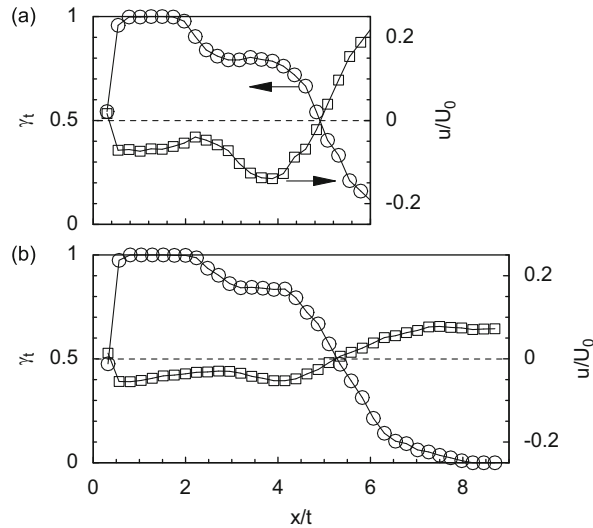
Fig. 5. Distribution of reverse flow intermittency and time-averaged streamwise velocity along $y/t = 0.6$: (a) $c/t = 6$ and (b) $c/t = 9$.
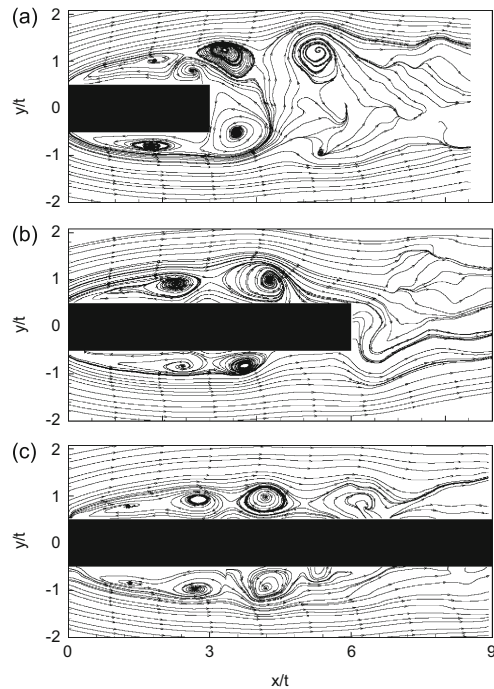

Fig. 6. A realization of the instantaneous streamline pattern: (a) $c/t = 3$, (b) $c/t = 6$ and (c) $c/t = 9$.

separation bubble that is always attached on the plate, gives rise to strong variation of the reverse flow intermittency in the range $x/t > 4$ (Fig. 5(b)). In the reduced plate with $c/t = 3$ (Fig. 6(a)), an induced vortex forms above the trailing edge because of the sharp upward motion of the fluid in the rear part of the vortex centered at $x/t = 2$ and the downward motion of the fluid in the front part of the vortex centered at $x/t = 3.5$.

The influence of the leading-edge vortices on the separated shear layer is indicated by plotting the contour of the time-averaged streamwise velocity fluctuation intensity in Fig. 7. For the system with $c/t = 3$ (Fig. 7(a)), the streamwise velocity fluctuation intensity peaks at 38% along the dividing streamline (Fig. 3(a)) above the trailing edge. The bulk
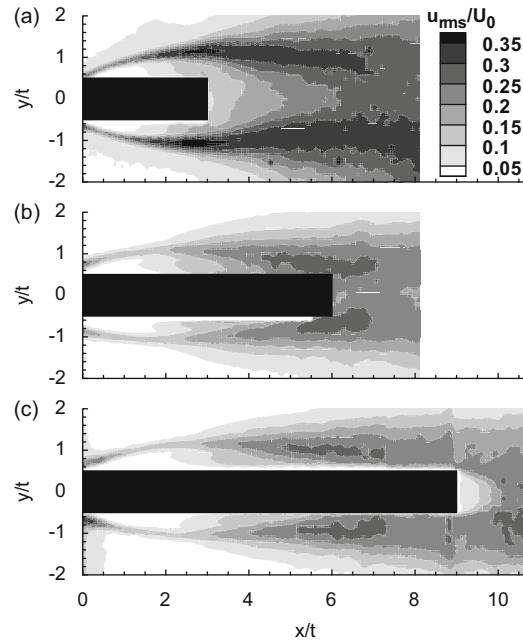
Fig. 7. Contour plot of the streamwise velocity fluctuation intensity: (a) $c/t = 3$, (b) $c/t = 6$ and (c) $c/t = 9$.
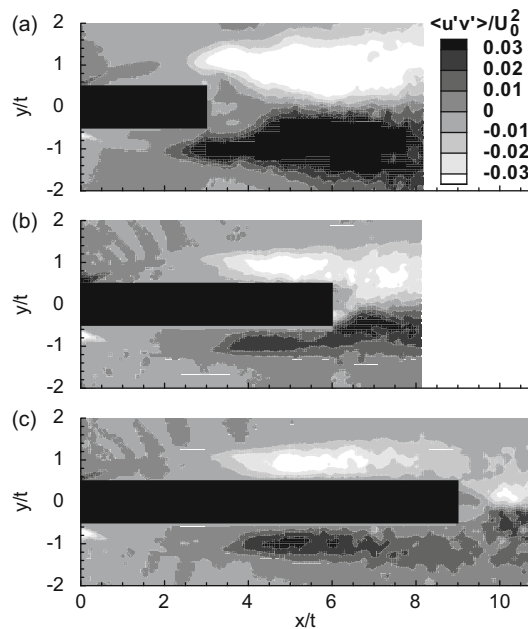

Fig. 8. Contour plot of shear stress: (a) $c/t = 3$, (b) $c/t = 6$ and (c) $c/t = 9$.

region between the separated shear layers features very low intensity. Far downstream from the trailing edge at $x/t = 8$, the fluctuation intensity remains at a high level of 32%; this indicates that the wake is highly unstable because of the interaction of the shedding vortices and occurrence of a Karman-like vortex street. With the increase of c/t, the peaked magnitude of the streamwise velocity fluctuation intensity in the coverage of the plate's surface is slightly reduced: it reaches 28% and 26% for the systems with $c/t = 6$ and 9, respectively. These values reflect the attenuation of the leading-edge vortices. In the system with $c/t = 6$ (Fig. 7(b)), the region of the intensified streamwise velocity fluctuation intensity at the near-wall is $x/t = 5$–7, which results from periodic reattachment of the separated shear layer. A similar

spatial pattern of the streamwise velocity fluctuation intensity is found in the system with $c/t = 9$, as shown in Fig. 7(c); the large fluctuation intensity region is defined by $x/t = 5$–7, which is closely associated with interaction between the large-scale vortices and the flapping separation bubble. As the fluid flows downstream from the reattachment zone, the fluctuation intensity tends to decrease because of decay of the leading-edge vortices that are buried in the redeveloping boundary layer. Of the three systems, the local streamwise velocity fluctuation intensity in the near-wake of the system with $c/t = 6$ is relatively large, 25%, because of the strong disturbance caused by the periodic reattachment of the separated shear layers to the trailing edge. In contrast to the system with $c/t = 6$, the near-wake fluid in the system with $c/t = 9$ is immune to the disturbance caused by the reattaching shear layer far upstream from the trailing edge, which significantly weakens the fluctuation intensity.

Fig. 8 displays the contour plot of the time-averaged shear stress normalized by the free-stream velocity. A general view of the shear stress distributions of the three systems distinctly exhibits the differences associated with the shedding motion of the vortices immersed in the separated shear layer. For the system with $c/t = 3$ (Fig. 8(a)), the shear stress intensifies as the leading-edge vortices of opposite vorticity are shed alternately into the wake, without the spatial limitation exerted by the plate surface. The growing vortices in the near-wake tend to interact near the station $x/t = 5$ and entrain more ambient fluid, which causes intensified shear stress. When the plate length is extended to $c/t = 6$, periodic reattachment of the vortices onto the plate surface causes increased shear stress of the fluid flow in the reattachment region and the near-wake region. The trail of the peaked shear stress immediately behind the trailing edge of the system with $c/t = 6$ is evidence of the growth of leading-edge vortices, which are shed directly into the wake during the non-reattachment phase. This process, combined with the contribution from the shedding vortices during the reattachment phase of the separated shear layers, causes dispersion of the large shear stress region behind the trailing edge. Further elongation of the plate to $c/t = 9$ does not increase the shear stress in the near-wake, which is attributed to decay of the leading-edge vortices in the redeveloping boundary layer.

The growth rate of the time-averaged separated shear layer was quantified using the vorticity thickness δ_ω as an unambiguous measure of the shear layer thickness

$$\delta_\omega = \frac{U_2 - U_1}{\partial \langle U \rangle / \partial y|_{\max}}, \tag{1}$$

where $\langle U \rangle$ is the time-averaged velocity, and U_2 and U_1 are the velocities of the upper and lower streams, respectively (Brown and Roshko, 1974). In the present work, U_2 is set equal to the free-stream velocity U_0, while U_1 is set to zero. Fig. 9 displays variation of the vorticity thickness of the shear layer with respect to the streamwise coordinates. As shown in Fig. 9, the curve for the system with $c/t = 6$ almost coincides with that for the system with $c/t = 9$ in the range of $x/t = 0$–5.5. The growth rate of the vorticity thickness $(d\delta_x/dx)$ for the system with $c/t = 3$ is slightly larger than that for the other two systems (in which $c/t = 6$ and 9); this phenomenon is attributed to the rapid growth of the vortices shed from the leading edge in the system with $c/t = 3$, which is also reflected in the distribution of the time-averaged streamwise velocity fluctuation intensity (Fig. 7). For the system with $c/t = 9$, the growth rate of the vorticity thickness $(d\delta_x/dx)$ is low near the leading edge, but it increases as the fluid moves downstream from the station $x/t = 4$ and reaches the approximately constant value 0.36. As the vortices emanate from the leading edge and convected
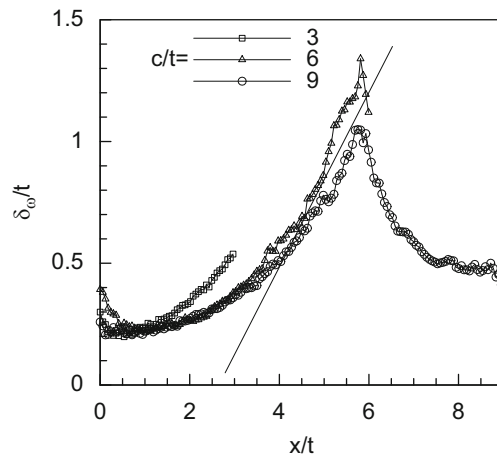
Fig. 9. Distribution of the shear layer vorticity thickness above the plate.

downstream, the growth of the vortices results in fast growth of the shear layer. For the system with $c/t = 9$, the vorticity thickness peaks near the station $x/t = 5.5$ because of the reattachment of the separated shear layer. Behind the reattachment point, the newly redeveloped boundary layer interacts strongly with the plate surface (Kiya and Sasaki, 1985), which causes the vortices immersed in the boundary layer to decay and increases the mean shear near the plate surface; correspondingly, the vorticity thickness decreases rapidly, as shown in Fig. 9.

3.3. Characteristics of the leading-edge vortices

To further understand the spatial characteristics of the vortices buried in the separated shear layer, we identify the large-scale vortices by spatially filtering the small-scale background 'noise' or turbulence. To achieve this, proper orthogonal decomposition (POD), which is used to extract a basis for modal decomposition from an ensemble of signals, was employed. In the present study, the analysis was implemented using snapshot POD (Sirovich, 1987). Detailed information regarding the principle and algorithm of snapshot POD has been described by Sirovich (1987). A total ensemble of 500 instantaneous vector fields is supplied for POD analysis. The zone $(0 < x/t < c/t; 0.5 < y/t < 2)$ was selected for calculation to ensure that the extracted flow energy is mostly concentrated on the low-order POD modes. The sensitivity of the low-order POD mode energy to the ensemble size M was tested for each case using data subsets with various sizes; the results without documentation reveal that the eigenvalue magnitudes of the low-order POD modes $(n < 5)$ do not vary obviously for M larger than 200, which indicates that the present ensemble size is sufficiently large to provide results that converge statistically. Fig. 10 displays the variation of normalized eigenvalues with respect to the first 50 POD modes. For all the systems, the eigenvalue rapidly decreases as the POD mode increases up to 10, while the eigenvalue does not appear to change as the mode number increases further. It is important to note that the first POD mode for the system with $c/t = 3$ is the major contributor (55.7%) to the total fluctuating energy because of the overwhelming dominance of the growing leading-edge vortices in the separated shear layer. However, the contribution of the first POD mode to the total fluctuating energy is low, 17.8% and 13.9%, for the systems with $c/t = 6$ and 9, respectively. In contrast to the system with $c/t = 3$, the considerable decrease in the first POD eigenvalue for the other two systems results from the spatially constrained growth of the leading-edge vortices buried in the reattached separated shear layer.

By reconstructing the flow field using the low-order POD modes, we can filter out small-scale fluctuations such that only the large-scale energy structures remain. The criteria for truncating the POD sequence is retention of the number of modes that capture more than 90% of the total fluctuating energy, while none of the neglected modes has more than 1% of the energy in the most energetic mode (Rehimi et al., 2008). To visualize the discrepancy between the reconstructed flow field and the original, an instantaneous realization of the separated shear layer in the system with $c/t = 3$ was spatially filtered by reconstructing the flow field using the first 6, 10 and 22 eigenmodes, which contribute 80%, 85% and 90% to the total fluctuation energy, respectively. The streamline patterns of the reconstructed flow fields and the original are shown in Fig. 11. The reconstructed flow field using the first 6 eigenmodes (Fig. 11(a)) can roughly predict the large-scale features of the flow structure. However, the smaller structure, which is evident near the position $(x/t = 1.3, y/t = 0.5)$ in the original flow field (Fig. 11(d)), cannot be observed in the reconstructed flow field using the first six eigenmodes. Adding additional eigenmodes (up to 10) for reconstruction does not cause a significant difference, as shown in Fig. 11(b). However, the reconstructed flow field using the first 22 eigenmodes (Fig. 11(c)) can represent the overall features of the original field. Thus, the velocity fields of the PIV measurements in the subsequent discussion were all spatially filtered by reconstructing the dominant POD eigenmodes containing 90% of the total fluctuating energy.

The spatial characteristics of the leading-edge vortices buried in the separated shear layer can be identified using two-point spatial correlation coefficients of velocity fluctuations. Previous studies that focused on the separated shear
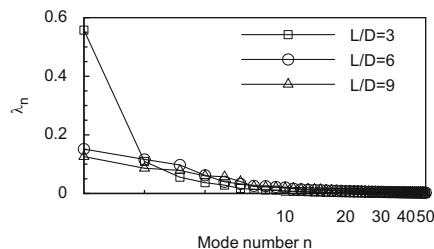

Fig. 10. Normalized eigenvalues for the first 50 POD eigenmodes.
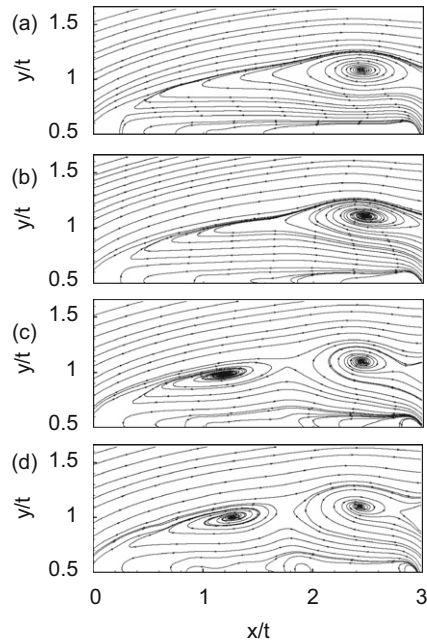
Fig. 11. Reconstructed flow field using different numbers of POD eigenmodes: (a) 6, (b) 10, (c) 22 and (d) all (original flow field).
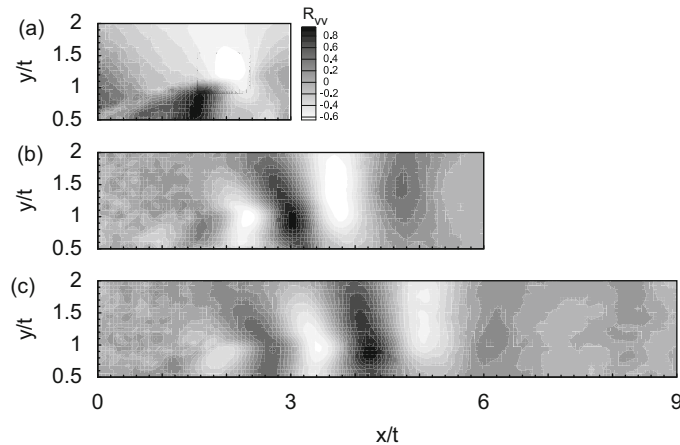

Fig. 12. Contour plot of spatial v–v correlation coefficient in reference to $(x_0/c = 0.5, y_0/t = 0.8)$: (a) $c/t = 3$, (b) $c/t = 6$ and (c) $c/t = 9$.

layer behind a cavity have described the vortices in terms of an alternating pattern of positive and negative correlation coefficients (Kang et al., 2008). In this study, we examined the spatial correlation coefficient of the fluctuating vertical velocity component above the plate surface

$$R_{vv}(x, y; x_0, y_0) = \frac{\langle v(x, y)v(x_0, y_0)\rangle}{v_{\mathrm{rms}}(x, y)v_{\mathrm{rms}}(x_0, y_0)}, \tag{2}$$

where (x_0, y_0) represents the reference point. Here, the reference position is determined to be $(x_0 = c/2, y_0 = 0.8t)$. Recall that the fluctuating vertical velocity components in Eq. (2) are all spatially filtered using the above-mentioned POD method to remove noisy spots in the correlation distribution, which are associated with small-scale behavior; thus, the distribution of the v–v correlation coefficients can be discussed in terms of the large-scale vortices. As shown in Fig. 12,
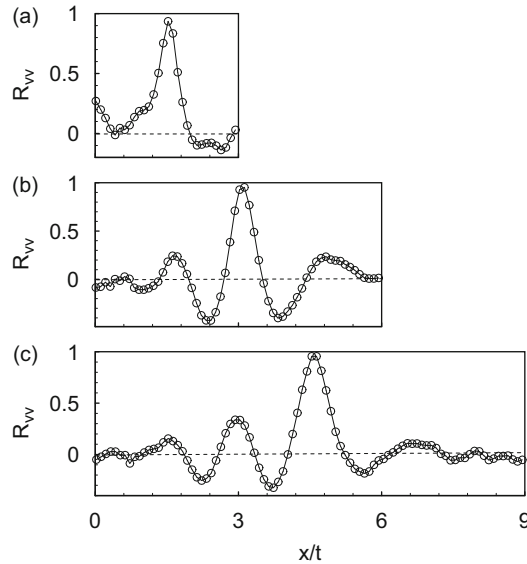
Fig. 13. Variation of spatial v–v correlation coefficient along $y_0/t = 0.8$ in reference to ($x_0/c = 0.5$, $y_0/t = 0.8$): (a) $c/t = 3$, (b) $c/t = 6$ and (c) $c/t = 9$.

an alternating pattern of positive and negative correlation coefficients is observed for all three systems, which represents an organized collection of large-scale vortices (Little et al., 2007). An examination of the high correlation area centered at the reference point for the system with $c/t = 6$ shows that there is a main ridge of positive correlation inclined at an angle, and two negative zones on either side of the main ridge. The scale of the high positive correlation area near the reference position reflects the spatial extent of the leading-edge vortices at the middle station of the plate. However, expansion of the other concentrated positive correlation area, which is centered at the position ($x/t = 4.8$, $y/t = 1.5$) in the reattachment zone, as shown in Fig. 12(b), is attributed to the rapid growth of leading-edge vortices. A detailed view of the contour patterns of the two concentrated positive correlation areas shows that the structure of the leading-edge vortices varies from backward to forward inclination when convected downstream. When the plate is elongated to $c/t = 9$, a large area of concentrated positive correlation is located near the position ($x/t = 7$, $y/t = 2$), while the considerably reduced correlation magnitude results from vortex decay in the redeveloping boundary layer. In addition, another concentrated positive correlation area is located at the upstream position ($x/t = 3$, $y/t = 1$), as shown in Fig. 12(c). In the system with the reduced chord-to-thickness ratio $c/t = 3$, shown in Fig. 12(a), the highly concentrated positive correlation zone centered at the reference position is closely contained below the dividing streamline (Fig. 3(a)).

Interestingly, Fig. 12 illustrates that the number of the changes between positive and negative correlation coefficients increases as the chord-to-thickness ratio increases. To closely inspect these changes, the streamwise distributions of the spatial correlation coefficients along $y_0/t = 0.8$ were extracted from Fig. 12 for the three systems and plotted in Fig. 13. For the system with $c/t = 3$ shown in Fig. 13(a), a single positive peak is observed at the reference position, while a single negative peak is found near the trailing edge; the considerably low magnitude of the negative peak might result from the contamination of unsteady near-wake behavior behind the trailing edge. For the longer plate with $c/t = 6$, three dominant positive peaks and two dominant negative peaks are observed, which form two full cycles. Similarly, four dominant positive peaks and three dominant negative peaks are found for the system with $c/t = 9$ in Fig. 13(c). The number of changes corresponds to the number of vortices formed in the coverage of the plate surface, which is in accordance with the previous findings (Ohya et al., 1992; Hourigan et al., 1993). Furthermore, the distance between two consecutive positive or negative peaks corresponds to the streamwise wavelength of the leading-edge vortices (Kang et al., 2008). Here, the streamwise wavelength λ_x is calculated to be $\lambda_x/t = 1.5$ for the system with $c/t = 6$. The two wavelengths determined from the streamwise distribution of the three negative peaks in the system with $c/t = 9$ (Fig. 13(c)) are determined to be $\lambda_x/t = 1.5$ and 1.9, which indicates that the convection speed of the large-scale vortices increases as the fluid flows downstream.

To accurately capture the spatial distribution of the large-scale vortices in the coverage of the plate surface, a more intuitive view can be derived by examining the instantaneous distribution of swirling strength (λ_{ci}), which is an effective measure to identify vortices in turbulent flows (Kang et al., 2008; Lee et al., 2008). The swirling strength is defined
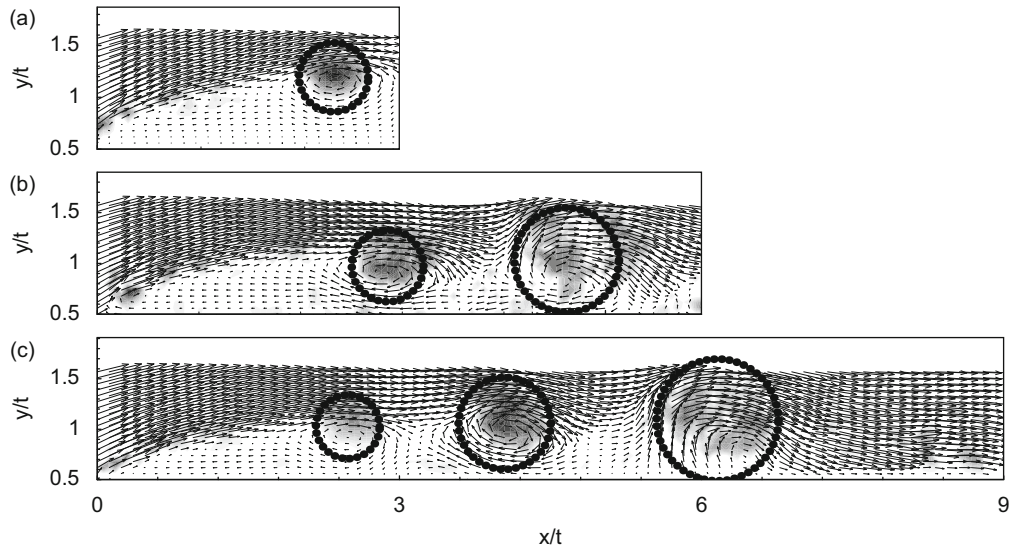
Fig. 14. Contour plot of the swirling strength of an instantaneous velocity field: (a) $c/t = 3$, (b) $c/t = 6$ and (c) $c/t = 9$.

as the imaginary part of the complex eigenvalue of the velocity gradient tensor (Adrian et al., 2000)

$$D = \begin{bmatrix} \dfrac{\overline{\partial u}}{\partial x} & \dfrac{\overline{\partial u}}{\partial y} \\ \dfrac{\overline{\partial v}}{\partial x} & \dfrac{\overline{\partial v}}{\partial y} \end{bmatrix}. \tag{3}$$

The swirling strength is frame independent and capable of discriminating compact vortical cores from regions of intense shear. The vortices are readily identified by plotting the isocontours for $\lambda_{ci} > 0$ (Adrian et al., 2000; Kang et al., 2008). Fig. 14 shows the instantaneous velocity field with an embedded plot the swirling strength contours. As denoted by the dotted circles in Fig. 14, one, two and three vortices form above the plate for the systems with $c/t = 3$, 6 and 9, respectively. The number of vortices distributed over the plate's surface for each system is similar to previously reported numerical results (Ohya et al., 1992). For the shortest plate ($c/t = 3$), a single vortex is detected at $x/t = 2.3$ that does not reattach to the plate surface. For the elongated plate ($c/t = 6$), a small vortex is located at the station $x/t = 2.8$, which induces a strong reversal flow in the near-wall region; at the downstream station $x/t = 4.6$, a larger vortex with reattachment to the wall forms, which gives rise to strong downward motion of the fluid to the trailing edge. For the longest plate ($c/t = 9$), a weak vortex is located at the station $x/t = 2.5$, while a stronger vortex is found at the station $x/t = 4.0$; in the separated shear layer reattachment zone, a very large vortex is disrupted near the station $x/t = 6.1$, while no clear trail of vortices is observed in the redeveloping boundary layer.

4. Conclusions

In the present study, the influence of the chord-to-thickness ratio (c/t) on the spatial characteristics of the separated shear layer over a blunt plate and the embedded leading-edge vortices was studied extensively using planar particle image velocimetry. Three systems corresponding to different shedding modes were chosen for comparison with a Reynolds number $Re_t = 1 \times 10^3$: $c/t = 3$, 6 and 9. The spatial characteristics of the separated shear layer were analyzed in terms of the time-averaged and instantaneous streamlines, distributions of the reverse flow intermittency, streamwise velocity fluctuation intensity and shear stress, and the vorticity thickness of the shear layer over the plate. The results show that the separated shear layer in the system with $c/t = 3$ does not reattach to the plate surface, while the wake behind the trailing edge is highly unstable because the leading-edge vortices shed directly into the wake. The time-averaged reattachment points for the systems with $c/t = 6$ and 9 were determined to be $x/t = 4.9$ and 5.3, respectively. The separated shear layer of the system with $c/t = 6$ periodically reattached to the plate surface, which caused increased fluctuations in the near-wake behind the trailing edge. In the longest system ($c/t = 9$), the separated shear layer always reattaches to the plate's surface far from the trailing edge, which

does not induce large fluctuations of the near-wake. The deviation of the growth rate of the vorticity thickness in the system with $c/t = 3$ from that of the other two systems is probably due to rapid vortex growth. To reveal the spatial characteristics of the leading-edge vortices above the plate surface, the original velocity fields were spatially filtered for further analysis by reconstructing the flow field using the POD eigenmodes that contain 90% of the total fluctuating energy. Subsequently, the alternating pattern of the positive and negative v–v correlation coefficients of the spatially filtered flow fields represented the organized large-scale vortices buried in the separated shear layer well. The number of changes between positive and negative coefficients was confidently determined to be 1, 2 and 3 for the systems with $c/t = 3$, 6 and 9, respectively. Distributions of the swirling strength of the separated shear layer accurately determined the position and structure of the large-scale vortices formed above the plate surface.

Acknowledgements

References

Adrian, R.J., Christensen, K.T., Liu, Z.C., 2000. Analysis and interpretation of instantaneous turbulent velocity fields. Experiments in Fluids 29, 275–290.

Brown, G.L., Roshko, A., 1974. On density effects and large structures in turbulent mixing layer. Journal of Fluid Mechanics 64, 775–816.

Hourigan, K., Mills, R., Thompson, M.C., Sheridan, J., Dilin, P., Welsh, M.C., 1993. Base pressure coefficients for flows around rectangular plates. Journal of Wind Engineering and Industrial Aerodynamics 49, 311–318.

Hourigan, K., Thompson, M.C., Tan, B.T., 2001. Self-sustained oscillations in flows around long blunt plates. Journal of Fluids and Structures 15, 387–398.

Kang, W., Lee, S.B., Sung, H.J., 2008. Self-sustained oscillations of turbulent flow over an open cavity. Experiments in Fluids 4 (45), 693–702.

Kiya, M., Sasaki, K., 1985. Structure of large-scale vortices and unsteady reverse flow in the reattaching zone of a turbulent separation bubble. Journal of Fluid Mechanics 154, 463–491.

Lee, S.H., Kim, J.H., Sung, H.J., 2008. PIV measurements of turbulent boundary layer over a rod-roughened wall. International Journal of Heat and Fluid Flow 29, 1679–1687.

Little, J., Debiasi, M., Caraballo, E., Samimy, M., 2007. Effects of open-loop and closed-loop control on subsonic cavity flows. Physics of Fluids 19, 065104.

Liu, Y.Z., Kang, W., Sung, H.J., 2005. Assessment of the organization of a turbulent separated and reattaching flow by measuring wall pressure fluctuations. Experiments in Fluids 38, 485–493.

Mills, R., Sheridan, J., Hourigan, K., 2003. Particle image velocimetry and visualization of natured and forced flow around rectangular cylinders. Journal of Fluid Mechanics 478, 299–323.

Nakamura, Y., Nakashima, M., 1986. Vortex excitation of prisms with elongated rectangular H and ⊢ cross sections. Journal of Fluid Mechanics 163, 149–169.

Nakamura, Y., Ohya, Y., Tsuruta, H., 1991. Experimental on vortex shedding from flat plates with square leading and trailing edges. Journal of Fluid Mechanics 222, 437–447.

Nakamura, Y., Ohya, Y., Ozono, S., Nakayama, R., 1996. Experimental and numerical analysis of vortex shedding from elongated rectangular cylinders at low Reynolds number $200\text{-}10^3$. Journal of Wind Engineering and Industrial Aerodynamics 65, 301–308.

Naudascher, E., Rockwell, D., 1994. Flow induced vibrations—an engineering guide. A.A.Balkema.

Ohya, Y., Nakamura, Y., Ozono, S., Tsuruta, H., Nakayama, R., 1992. A numerical study of vortex shedding from flat plates with square leading and trailing edges. Journal of Fluid Mechanics 236, 445–460.

Parker, R., Welsh, M.C., 1983. Effects of sound on flow separation from blunt flat plates. International Journal of Heat and Fluid Flow 4, 113–127.

Rehimi, F., Aloui, F., Nasrallah, S.B., Doubliez, L., Legrand, J., 2008. Experimental investigation of a confined flow downstream of a circular cylinder centered between two parallel walls. Journal of Fluids and Structures 24, 855–882.

Sirovich, L., 1987. Turbulence and the dynamics of coherent structures. Quarterly of Applied Mechanics 45, 561–590.

Stokes, A.N., Welsh, M.C., 1986. Flow-resonant sound interaction in a duct containing a plate. II: square leading edge. Journal of Sound and Vibration 104, 55–73.

Westerweel, J., Dabiri, D., Gharib, M., 1997. The effect of a discrete window offset on the accuracy of cross-correlation analysis of digital PIV recordings. Experiments in Fluids 23, 20–28.

Yaghoubi, M., Mahmoodi, S., 2004. Experimental study of turbulent separated and reattached flow over a finite blunt plate. Experimental Thermal and Fluid Science 29, 105–112.

Yasuhiko, S., Nishio, Y., Okuno, T., Okamoto, K., 2000. A highly accurate iterative PIV technique using a gradient method. Measure Science and Technology 11, 1666–1673.